A Hybrid Simulation Model for Electromagnetic Launchers Including the Transient Inductance and Electromotive Force

A Hybrid Simulation Model for Electromagnetic Launchers Including the Transient Inductance and Electromotive Force

Nail Tosun, *Graduate Student Member, IEEE*, Hakan Polat, *Member, IEEE*, Doğa Ceylan, Mustafa Karagöz, Baran Yıldırım, İbrahim Güngen, and Ozan Keysan, *Member, IEEE*

***Abstract*— Although electromagnetic launchers (EMLs) are superior to classical gun-powder-based launchers, they have to withstand extreme electrical and mechanical conditions. Therefore, the optimal design and precise simulations of these devices are crucial. In this article, a new simulation strategy for EMLs is proposed in order to achieve high accuracy and reduced complexity. The inductance and electromotive force (EMF) variations in the transient, which have a considerable influence on the launch process, are modeled using the finite element method (FEM) coupled with electrical circuit simulation. The proposed method has a good agreement with the experimental results of two EMLs (EMFY-1 and EMFY-2), which have 25- and 50-mm square bores and 3-m-length launchers. The study showed that the hybrid model with transient inductance and EMF calculations showed a good agreement with experiments that have 625 kJ–3.241-MJ input energies.**

***Index Terms*— Electromagnetic launchers (EMLs), electromotive force (EMF), finite element method (FEM), pulse power supplies, transient inductance, velocity skin effect (VSE).**

I. Introduction

THE electromagnetic launcher (EML) is a linear electromechanical energy conversion device which is used to accelerate a projectile to a few thousand meters per second. The standard EMLs have two rails and an armature. The armature accelerates the projectile, and sabot petals provide its mechanical support to maintain it between the rails. Pulse power supply (PPS) generates a pulse-shaped current in the order of a few million amperes [1], [2]. Such a large current in the system creates significant pressure and temperature gradients, which are difficult to withstand. Therefore, a realistic simulation model is crucial for both the design and operation process of EMLs.

In the early versions of EML, simulation codes consisted of lumped circuit models [3]–[5] and finite element methods (FEMs) [6]. These lumped circuit models are coupled with kinematic equations to take into account the change in the inductance and resistance due to the armature motion. However, geometries of the rails and armature are kept as simple as possible since analytical formulations are used. FEM is an excellent alternative to include the effect of armature and rail geometries. However, the aspect ratio of an EML is high due to the long rails compared to the small rail cross section. For this reason, the analysis of EMLs using FEM requires a large number of mesh elements for accurate results [7]. On top of that, 3-D FEM simulations with a moving armature are even more complicated to compute due to high-velocity sliding electrical contacts [8]. Thus, commercial programs are not fully capable of simulating the sliding electrical contacts between the armature and rails [8]. To overcome these problems, there are mainly two different approaches in the literature. Several researchers [9]–[11] built special FEM codes to model EMLs without using commercial software. However, these studies require specific knowledge of numerical computation. Building a 3-D FEM simulation code from scratch is quite time-consuming [12]. Other researchers used commercial FEM codes rather than special ones and utilized different techniques to model phenomena, which commercial codes are not able to model inherently, such as velocity skin effect (VSE). Solving the VSE problem accurately in transient and 3-D is not possible using commercial FEM packages due to the continuity conditions at the interface between static and moving mesh elements. However, 2-D transient FEM models can be used for investigating VSE phenomena [13]. The position and time-dependent conductivity is proposed in the rails to simulate the armature movement without using moving mesh structure [12], [14]. Moreover, time-harmonic solutions can also be to model the velocity-related current clustering without moving the armature [15], [16].

Ceylan *et al.* [17] used a 2-D-transient FEM method, which includes a moving armature to model a VSE resistance, which is later used to improve the 3-D static simulation environment. The position of the armature is calculated using kinematic equations excited with Lorentz force, and analytically modeled rail portion is added as a lumped circuit parameter. To model transient effects in the rails, these lumped parameters are updated at each time step using a 3-D FEM model.

In this study, a new hybrid 3-D FEM coupled electrical circuit simulation, which is enhanced with transient inductance

Manuscript received May 16, 2020; revised July 29, 2020; accepted August 11, 2020. Date of publication August 27, 2020; date of current version September 11, 2020. The review of this article was arranged by Senior Editor F. Hegeler. *(Corresponding author: Ozan Keysan.)*

Nail Tosun, Hakan Polat, Doğa Ceylan, and Ozan Keysan are with the Department of Electrical and Electronics Engineering, Middle East Technical University, 06800 Ankara, Turkey (e-mail: keysan@metu.edu.tr).

Mustafa Karagöz, Baran Yıldırım, and İbrahim Güngen are with ASELSAN Inc., 06370 Ankara, Turkey (e-mail: mkaragoz@aselsan.com.tr).

Color versions of one or more of the figures in this article are available online at http://ieeexplore.ieee.org.

Digital Object Identifier 10.1109/TPS.2020.3016930

TABLE I
GEOMETRIC PARAMETERS OF LAUNCHERS

	EMFY-1	EMFY-2
Rail thickness	20 mm	60 mm
Rail height	25 mm	60 mm
Rail separation	25 mm	50 mm
Rail length	3 m	3 m

Fig. 1. EMFY-1 EML [17].

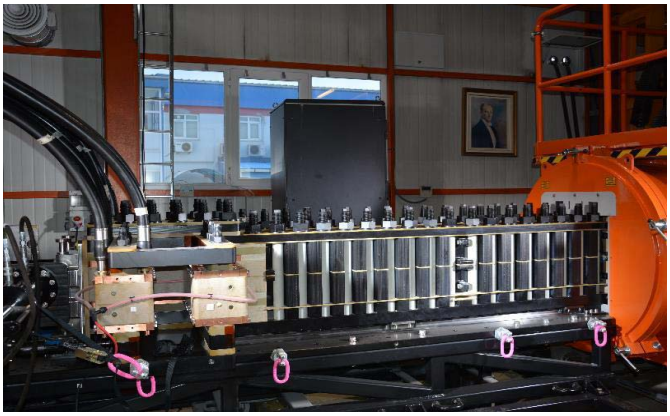

Fig. 2. EMFY-2 EML [18].

and a new electromotive force (EMF) calculation methods, is introduced. The proposed method includes the EMF related to the armature motion as well as the EMF due to rail current distribution change, which becomes dominant when larger rails are used. Moreover, 3-D quasi-transient FEM model that uses position and time-dependent conductivity to model armature motion is used to calculate VSE resistance. The derived VSE resistance is used to later enhance the hybrid model. The proposed method is implemented and verified experimentally with two different EMLs developed by ASELSAN [18]. The geometric parameters of which are given in Table I. The mechanical structure of EMFY-1 and EMFY-2 EMLs are presented in Figs. 1 and 2, respectively.

II. SIMULATION MODEL

The hybrid simulation model diagram is illustrated in Fig. 3. The hybrid model consists of a 3-D FEM model and a lumped circuit model, which is used to simulate PPS and rail portion that is not covered by the FEM model. Resistances and

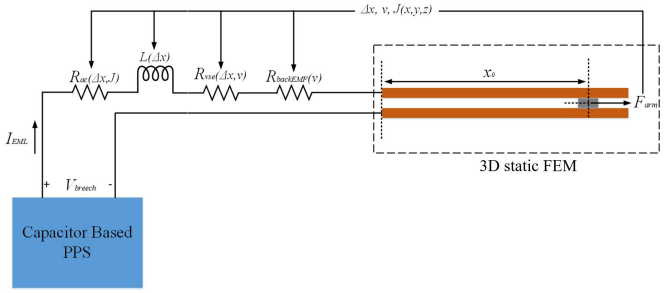

Fig. 3. Hybrid FEM model to simulate EMLs.

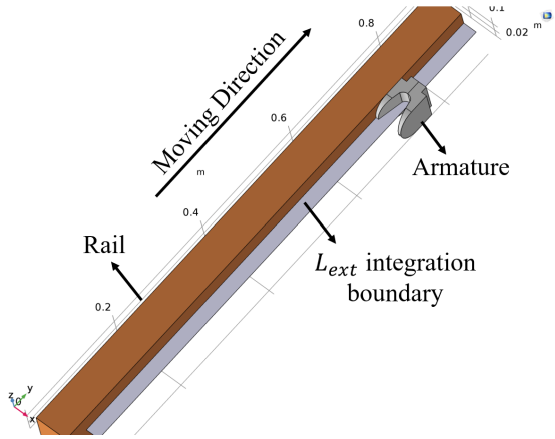

Fig. 4. Geometry which is used for 3-D FEM analysis of EMFY-2. Half symmetry is used for all FEM simulations. The integration boundary for L_{ext} is demonstrated.

inductances between the PPS network and 3-D FEM body are used to model the movement of the armature. With that structure, not only the computational complexity due to mesh movement is significantly decreased, but also the total number of mesh element is reduced.

In Fig. 4, the geometry used for 3-D FEM analysis is shown. It should be noted that armature is kept stationary at the preload position throughout the FEM simulation. The lumped circuit accurately models the inductance and resistance change due to the armature motion. The coupling between the two models is satisfied using the following kinematic equations. The Lorentz force which accelerates the armature obtained by 3-D FEM analysis where V_{arm} denoted as the volume of the armature

$$\vec{F}_{\text{arm}} = \iiint_{V_{\text{arm}}} \vec{J} \times \vec{B}\, dV \tag{1}$$

$$\Delta x = \int_0^t \int_0^t \frac{\vec{F}_{\text{arm}}}{m_{\text{arm}}}\, dt\, dt \tag{2}$$

Δx is the displacement of the armature from its initially preload position. The parameters which are used in the circuit simulation and their roles in the overall model are summarized in Section II-A–II-C.

A. EMF Calculation, $R_{backEMF}$

The EML can be considered a one turn coil with a time-dependent geometry

$$\Phi(t) = \lambda(t) = L(t)I(t). \tag{3}$$

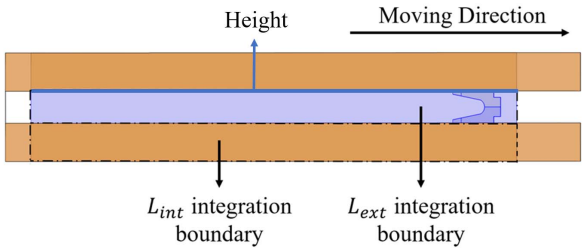

Fig. 5. Integration boundaries which are used for L_{ext} and L_{int} calculations. Inductance gradients, L'_{ext} and L'_{int} is calculated dividing the calculated inductance values with the height of the integration boundaries.

The EMF can be calculated using Lenz's Law

$$\epsilon(t) = \frac{d\lambda(t)}{dt} = \frac{dL(t)}{dt} I(t) + L(t)\frac{dI(t)}{dt}. \tag{4}$$

The first term in (4) is related to the transient inductance of the system. When the armature is considered as the only moving part, the total inductance of the system increases only with armature movement. Then, (4) can be reconstructed like in (5) and (6) in which velocity denoted as v is the armature velocity and L' is the inductance gradient. Although back EMF is not physically a resistance, it can be used in a mathematical model to represent the back EMF voltage

$$\epsilon(t) = \left(\frac{d}{dx}\frac{dx}{dt}L(t)\right) I(t) + L(t)\frac{dI(t)}{dt} \tag{5}$$

$$\epsilon(t) = vL'(t)I(t) + L(t)\frac{dI(t)}{dt} \tag{6}$$

L' can be derived using the Lorentz force on the armature as follows:

$$F_{\text{arm}} = \frac{1}{2}L'I^2 \tag{7}$$

$$L' = \frac{2F_{\text{arm}}}{I^2}. \tag{8}$$

Then the first part of the EMF equation can be used to model R_{backEMF} as given in (10)

$$\epsilon(t) = R_{\text{backEMF}} I(t) + L(t)\frac{dI(t)}{dt} \tag{9}$$

$$R_{\text{backEMF}}(t) = vL'(t). \tag{10}$$

The second term in (4) is the voltage on the EML inductance due to rail current transient. This inductance can be further divided into two parts: the interior inductance L_{int} and the exterior inductance L_{ext}. The integration surfaces which we used to calculate these inductance are demonstrated in Fig. 5.

When the R_{backEMF} is calculated in that way as in [17], the only term that affects the inductance change of the system is considered as the armature displacement. However, due to varying skin effect throughout the launch process, the current path in the rails also changes with time. This variation in the rail current path is responsible for an inductance change, which should be considered when the EMF term is evaluated. Especially for larger caliber launchers, the transient effect of the rail inductance becomes more dominant due the larger lateral rail current displacement. Then the EMF equation (4) should be reconsidered so that R_{backEMF} should be modeled like (11) without the assumption that the armature is responsible the inductance change only. The deviation of the equivalent current path in an EML is analogous with a coil that is deformed as shown in Fig. 6

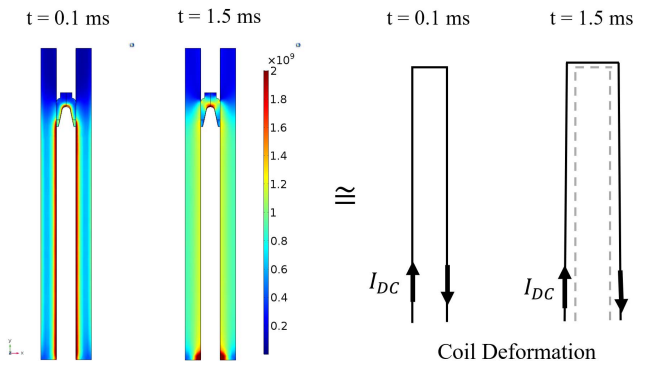

Fig. 6. Coil deformation analogy. Transition from highly transient rail current to dc state can be considered as lateral deformation of a coil. Changing in the rail current path creates a transient inductance change which is also a source of EMF.

$$R_{\text{backEMF}}(t) = \frac{dL(t)}{dt}. \tag{11}$$

Even though constant current excitation is applied, there exists an induced EMF at the terminals of the coil when it is deformed, as shown in Fig. 6. At $t = 0.1$ ms, due to the initial firing of the PPS units, the current is highly transient, and the current is concentrated at the inner rail surface. However, later on the rail current reaches into dc state and gets a more homogeneous distribution. Lateral displacement of the rail current density can be considered as an expansion of a single turn coil. Therefore, when only inductance variation due to the armature movement is considered, the calculated EMF is less than the actual one, since the EMF contribution of the displacement of current distribution is ignored. EMF calculations with and without transient rail inductance for EMFY-1 and EMFY-2 are shown in Fig. 7. It should be noted that the proposed model has higher EMF resistance than the EMF resistance calculated with the control method since the proposed one also covers the rail inductance change. Since the rail thickness as presented in Table I is smaller for EMFY-1, the difference between methods is not significant as EMFY-2.

B. Inductance

While the armature moves through rails, the inductance of the system increases. However, 3-D FEM simulation calculates just the inductance of the system at the preload position since the model is static. Inductance contribution due to armature displacement added to the simulation using the lumped inductance parameters. The difference between these inductances arises from integration boundaries. Exterior boundary is used to calculate L_{ext}, which is due to change of the air region between the rails. Interior boundary is used to calculate L_{int}, which is then used to model the rail inductance with L_{ext}. Inductance gradients, which are calculated from 3-D FEM and the displacement which comes from kinematic equations

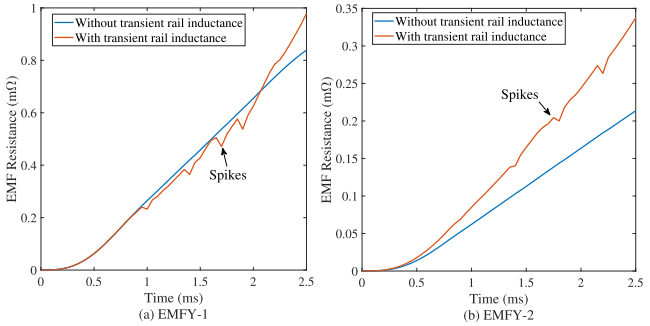

Fig. 7. Comparisons of the two calculation methods of EMF resistance on (a) EMFY-1 and (b) EMFY-2. The proposed method which uses (11) for EMF calculation, clearly gives a larger resistance than the method which uses (10) for EMF calculation, especially at EMFY-2. The reason for that is the fact that rail current movement is also included in the EMF calculation. Spikes at the EMF resistance where transient rail inductance included comes from the discrete derivative operator in (11).

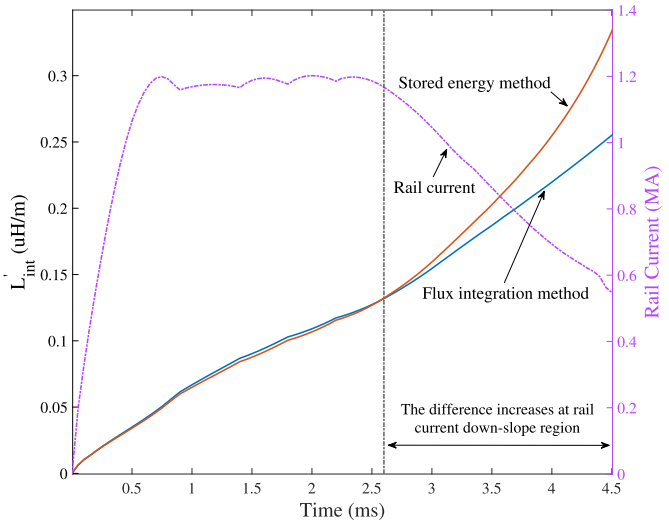

Fig. 8. Comparison of L_{int}. EMFY-2 simulation model used in these calculations. Difference between two model increases especially at the downslope rail current region.

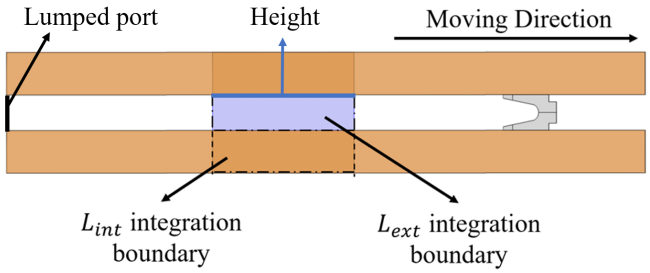

Fig. 9. New integration boundary for lumped inductance calculations. Armature is far away from the integration boundaries. The new integration boundaries are shorter than the previous ones. The reason for such a change is preventing both the effects of lumped port and armature from inductance gradient calculation. Since the calculated inductance value normalized with the height of the integration boundary, the height is an invariant parameter for inductance gradient calculation.

used to model the lumped inductance $L(t)$ as in the following equation:

$$L(t) = \left[L'_{\text{ext}}(t) + L'_{\text{int}}(t)\right]\Delta x(t). \tag{12}$$

In this part of the study, we developed two main contributions to inductance gradient calculation. The first one is about the methodology we used for lumped inductance calculation. We used two different methods to compute L_{int}, namely, the flux integration method and the stored energy method.

The flux integrating method use a surface integral on the inductance related area to integrate the rail flux. Then the inductance is calculated using (13) where A_{int} is the area of the interior inductance

$$L_{\text{int}}(t) = \frac{1}{I}\iint_{A_{\text{int}}} (B_z(t) > 0) B_z(t)\, dA_{\text{int}}. \tag{13}$$

The energy method uses the stored magnetic energy in the rails to compute inductance. The stored energy in rail is calculated as in (14) and (15) where V_{rail} is the volume of single rail

$$E_{\text{stored}}(t) = \iiint_{V_{\text{rail}}} \vec{H}(t)\vec{B}(t)\, dB = \frac{1}{2}L_{\text{int}}(t)I^2(t) \tag{14}$$

$$L_{\text{int}}(t) = \frac{2E_{\text{stored}}(t)}{I(t)}. \tag{15}$$

However, these two methods give slightly different results as shown in Fig. 8. L'_{int} calculations diverge especially at the downslope region of the rail current. The integration boundaries that used to compare these methods are illustrated in Fig. 9. This variation is explained in Fig. 10 using the current distribution and the magnetic flux density vectors. At $t = 0.5$ ms, current density is concentrated at the edges due to skin effect which is shown in Fig. 10(a). Therefore, there is a small magnetic field density inside the rail, which makes L_{int} minimal. Then, rail current starts to go into low-frequency state at $t = 1.5$ ms, which is shown in Fig. 10(b). Some of the magnetic flux density vectors in the rail close their loop through the air region. Therefore, when flux counting method is used, not only the rail inductance but also air inductance is calculated. The part of the L_{int} that comes from the air region cannot be calculated from the stored energy method since the volume integration includes only the rail.

It should be noted that both approaches for calculating L'_{int} are fundamentally true, but there is a slight difference in their definition. At $t = 4.75$ ms, the current in the downsloped phase, in which two factors are shaping in the current distribution. The first one is the skin effect due to current transient and the second one is the current diffusion process due to transition from dc to ac state. L_{int} is still high due to the inner current density. However, computed L_{int} from the stored energy method is a bit misleading since the current distribution at the edges contribute L_{ext} rather than L_{int} but the volume integration in (14) uses that in L_{int} calculation.

Ceylan *et al.* [17] used the integration domain illustrated in Fig. 3 that covers rail as well as the armature domains. However, this integration boundary brings error about inductance calculation when it is used in the lumped parameter calculation. The reason is that lumped inductance parameters are used to model inductance of the rail portion, which is not covered in 3-D FEM. Therefore, the current distribution

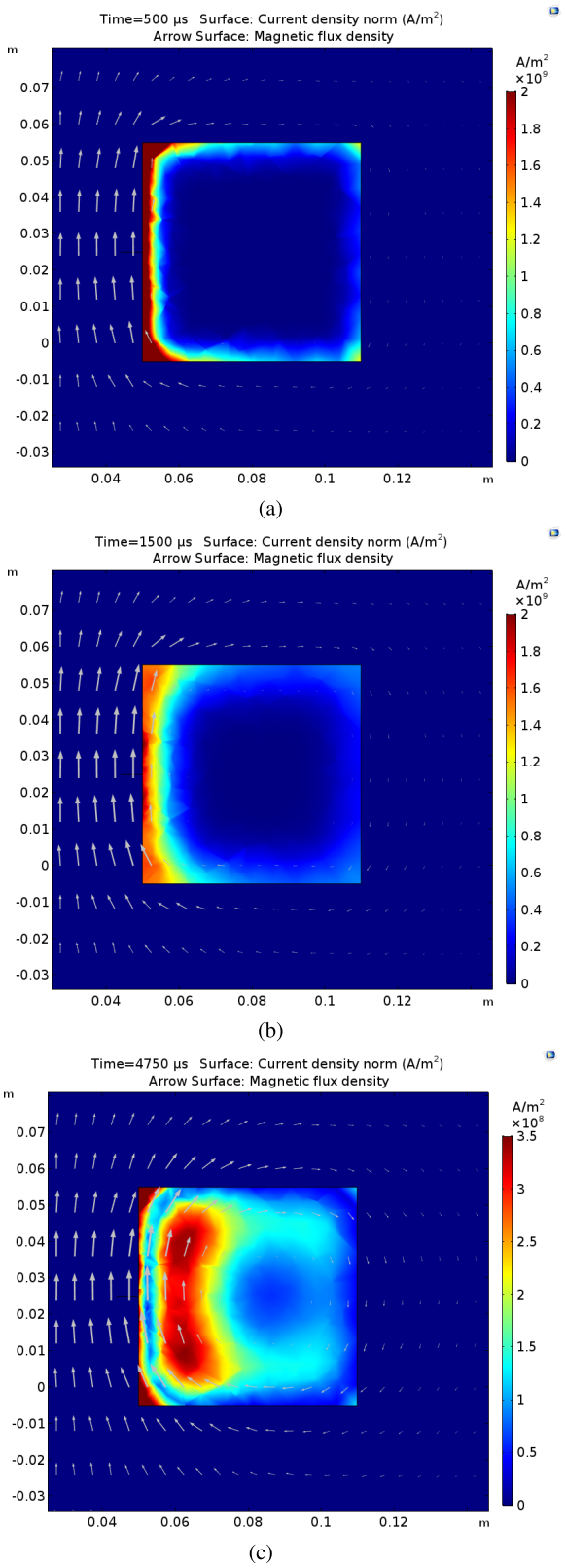

Fig. 10. Rail current distribution and magnetic flux density vectors throughout the launch. The color legend is for the current density only and its unit is A/m^2. The rail current waveform is demonstrated in Fig. 8. (a) 0.5, (b) 1.5, and (c) 4.75 ms.

should not be affected due to armature. The new integration area which excludes the armature is shown in Fig. 9. L_{ext} calculations with two different integration boundaries are shown

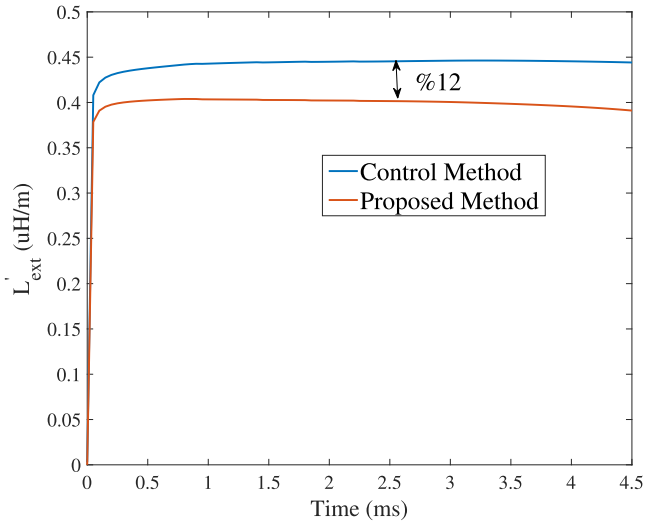

Fig. 11. Comparison of L'_{ext} calculation methods. Control method found inductance gradient %12 higher since the domain includes armature rail interaction region. Integration boundaries which are used in the control method and the proposed method can be seen in Figs. 3 and 7, respectively.

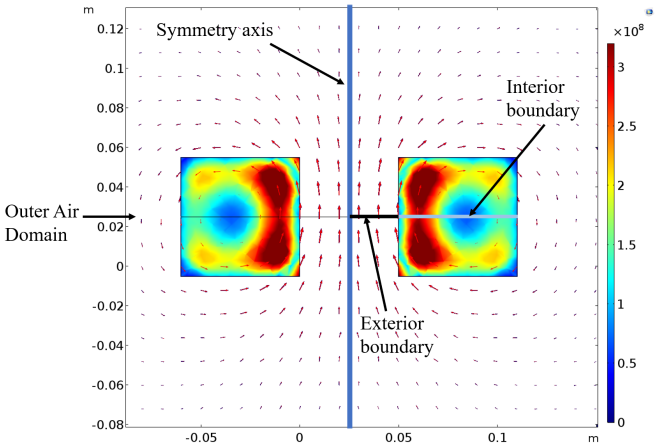

Fig. 12. Definitions of the interior and exterior boundaries, outer air domains, and the symmetry axis. There is a significant amount magnetic flux density around the outer air domain which is taken into account when the inductance are calculated. The color legend is for the current density only and its unit is A/m^2.

in Fig. 11. The new boundary which excludes the armature give 12% deficit in L_{ext} calculation. The outer air region, and interior and exterior boundaries are illustrated in Fig. 12.

C. VSE Modeling, R_{vse}

2-D transient FEM simulation is used to estimate VSE resistance, R_{vse} [17]. The reason for this is 3-D transient FEM analysis is hard to converge for EML simulations. In the proposed method, we used a quasi-transient 3-D FEM simulations to fit R_{vse} rather than 2-D approximation. In quasi-transient FEM analysis, the armature does not actually move, i.e., meshes of the armature are stationary. However, conductivity of air-armature region is modified with time in the direction of armature motion to simulate the movement. In Fig. 13, the moving armature-air conductivity function is

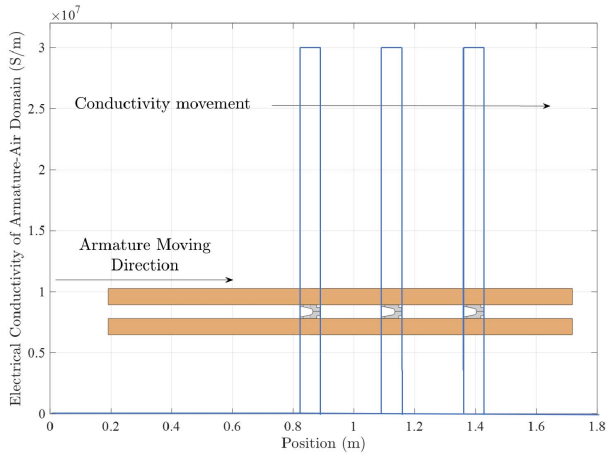

Fig. 13. Time and position dependent electrical conductivity function used in armature-air region.

represented. Such a method is called a Eulerian method [12], and it converges quickly in 3-D EML simulations.

It should be noted that 2-D approximation of fitting R_{vse} overestimates the actual VSE resistance. The reason is that 2-D approximation assumes that the rails and air have infinite height and the current distribution is identical through symmetry axis. However, 3-D rail geometry has rail–air boundaries. Thus, current distribution across to symmetry axis is not uniform. Under infinite rail height assumption, current clustering happens across to rail height which cause overestimation in VSE resistance calculation.

III. Results

In this section, the developed hybrid model which include transient inductance and EMF is compared with four experimental results. Two launch results of EMFY-1 and two launch results of EMFY-2 are represented. Two simulation methods are constructed to understand the improvements that mentioned in Section II. The proposed method regards improvements whereas the control method is used to create benchmark. Differences between the proposed and control methods are listed in the following.

1) The proposed method uses (11) for $R_{backEMF}$ calculation which covers the transient inductance related EMF. The control method uses (10) which only calculate armature related EMF.
2) Both the proposed and the control group methods use flux-integration method to calculate lumped inductance parameters. However, the proposed method uses armature excluded integration boundary which is shown in Fig. 9 whereas the control group uses armature included boundary which is given in Fig. 5.
3) The proposed method uses R_{vse} from 3-D quasi-transient analysis whereas the control group uses R_{vse} from 2-D transient analysis which used in [17].

Rail currents measured with Rogowski coils for both EMFY-1 and EMFY-2 launchers. The muzzle velocity of the launch package is measured by high-speed camera. Armature exit time can also be used to verify the kinematic calculations

TABLE II
Parameters of EMFY-1 and EMFY-2 Experiments

	EMFY-1		EMFY-2	
	Exp. A	**Exp. B**	**Exp. C**	**Exp D.**
Initial Electrical Energy	750 kJ	625 kJ	1.227 MJ	3.241 MJ
Launch Package Mass	41.4 g	41.6 g	932 g	1033.2 g
Capacitor Voltage	3560 V	3250 V	4000 V	6500 V

TABLE III
Error Analysis[1] of Rail Current Waveform

Experiment No	Control Method	Proposed Method
EMFY-1 Experiment A	73.29 kA	18.4 kA
EMFY-1 Experiment B	19.61 kA	4.61 kA
EMFY-2 Experiment C	49.58 kA	18.57 kA
EMFY-2 Experiment D	99.13 kA	22.65 kA

[1] RMSE error which we defined in (16) used in this analysis.

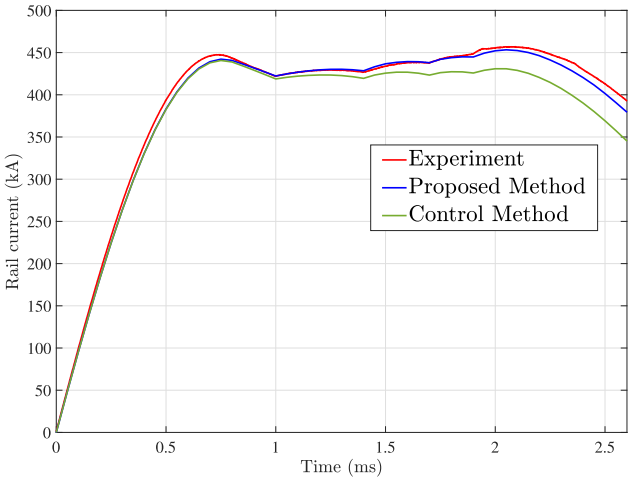

Fig. 14. Simulation and experimental results for the rail current of the experiment-A. EMFY-1 launcher is used in this experiment.

of the proposed model. Experimental parameters of EMFY-1 and EMFY-2 are given in Table II.

A. EMFY-1 Experiments

EMFY-1 is the first EML developed with a C-type solid aluminum armature powered by 4-MJ capacitor-based PPS [17]. The launch tests of EMFY-1 were conducted in open area in 2018. The proposed model is compared with two EMFY-1 experiments, with stored electrical energies of 750 and 625 kJ. The schematic and parameters of PPS which is used in these experiments can be found in [19]. The simulations and experiment rail current waveforms comparison for EMFY-1 launcher is given in Figs. 14 and 15.

B. EMFY-2 Experiments

EMFY-2 is the second EML developed by ASELSAN Inc. [18]. The launch tests were conducted in ASELSAN electromagnetic launch laboratory in Ankara in 2019. Thirteen 250-kJ PPS modules were used in parallel. The stored electrical energy for the EMFY-2 experiments are 1227 and 3241 kJ, respectively. EMFY-2 experiments are compared with the simulations in Figs. 16 and 17.

TABLE IV
SOME CRITICAL OUTPUTS OF THE EMFY-1 AND EMFY-2 EXPERIMENTS AND SIMULATIONS WITH THE CONTROL AND PROPOSED METHODS

	Proposed Method	Control Method	Experimental Result	Improvement[1]
EMFY-1 Experiment A				
Peak Rail Current	453 kA	444 kA	457 kA	2.84%
Muzzle Current	368 kA	325.1 kA	354 kA	4.21%
Armature Exit Time	2.7 ms	2.82 ms	2.75 ms	0.70%
Muzzle Velocity	2220 m/s	2062 m/s	2174 m/s	3.04%
Muzzle Kinetic Energy	102.02 kJ	88.44 kJ	98.30 kJ	6.25%
Efficiency	13.60%	11.79%	13.11%	6.25%
EMFY-1 Experiment B				
Peak Rail Current	404 kA	401 kA	409 kA	0.73%
Muzzle Current	306 kA	282 kA	303 kA	5.94%
Armature Exit Time	2.99 ms	3.1 ms	2.98 ms	0.32%
Muzzle Velocity	1891 m/s	1744 m/s	1973 m/s	7.45%
Muzzle Kinetic Energy	74.74 kJ	63.26 kJ	80.96 kJ	14.18%
Efficiency	11.96%	10.12%	12.90%	14.18%
EMFY-2 Experiment C				
Peak Rail Current	1046 kA	1055 kA	1039 kA	0.87%
Muzzle Current	239 kA	309 kA	272 kA	1.47%
Armature Exit Time	5.99 ms	6.14 ms	5.90 ms	2.54%
Muzzle Velocity	577 m/s	576 m/s	627 m/s	0.15%
Muzzle Kinetic Energy	155.14 kJ	154.61 kJ	199.31 kJ	0.27%
Efficiency	12.65%	12.62%	16.24%	0.27%
EMFY-2 Experiment D				
Peak Rail Current	1202 kA	1222 kA	1202 kA	1.66%
Muzzle Current	564 kA	657 kA	595 kA	5.21%
Armature Exit Time	4.51 ms	4.65 ms	4.40 ms	2.37%
Muzzle Velocity	928 m/s	920 m/s	1020 m/s	0.78%
Muzzle Kinetic Energy	444.47 kJ	436.78 kJ	585 m/s	1.31%
Efficiency	13.71%	13.48%	18.08%	1.31%

[1] Improvement ratio is described at (18).

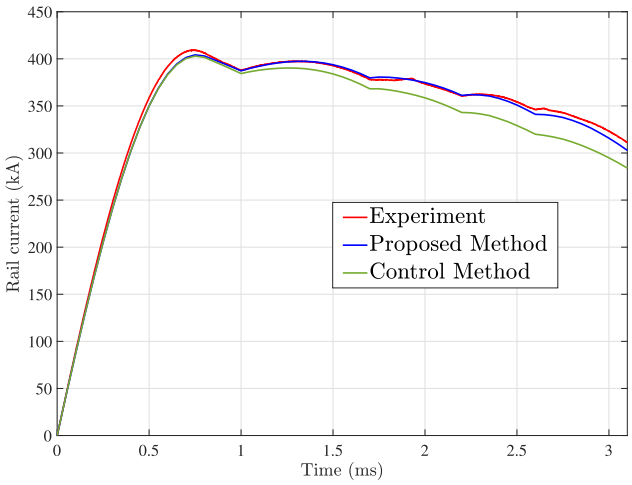

Fig. 15. Simulation and experimental results for the rail current of the experiment-B. EMFY-1 launcher is used in this experiment.

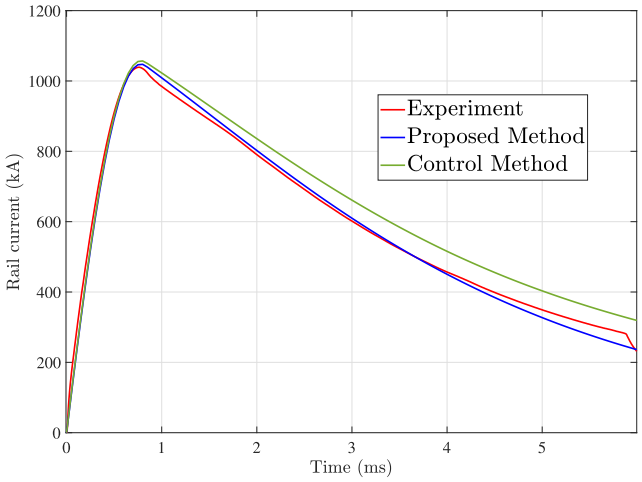

Fig. 16. Simulation and experimental results for the rail current of the experiment-C with EMFY-2 launcher.

C. Comparison

Root-mean square error (RMSE) of the current waveforms which is obtained from simulations and experiments are given in Table III. Error formulation that we used in current waveform analysis is given in (16) where n, $\hat{x}$, and x represent the amount of the sampled data, simulated value, and experimental value, respectively. The simulation results of the control method, proposed method, experimental results, and improvement ratios (IRs) are given in Table IV. IR which we used to compare two methods uses mean absolute error (MAE) of the measurement parameters such as armature exit time, muzzle current, and muzzle speed. MAE and the IR are defined in (17) and (18), respectively, where $\hat{x}_{\text{control}}$, $\hat{x}_{\text{proposed}}$ and x represent the simulated value of control method, the simulated value of proposed method, and experimental result, respectively

$$\text{RMSE} = \sqrt{\frac{1}{n}\sum_{i=1}^{n}(\hat{x}-x)^2} \tag{16}$$

$$\text{MAE} = |\hat{x}-x| \tag{17}$$

$$\text{IR} = \frac{\text{MAE}(\hat{x}_{\text{control}}, x) - \text{MAE}(\hat{x}_{\text{proposed}}, x)}{x}. \tag{18}$$

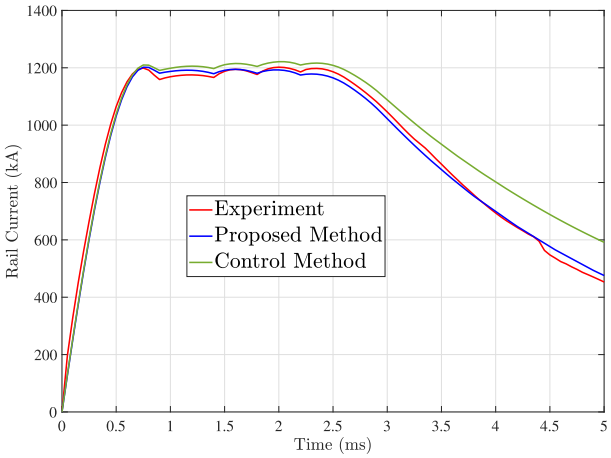

Fig. 17. Simulation and experimental results for the rail current of the experiment-D with EMFY-2 launcher.

The proposed method showed that transient inductance and EMF calculations improved the simulation-experiment accuracy by 3.49% in average. Moreover, the rail current waveforms fit the experimental results better which indicate the inductance and resistances of the systems are found better with the proposed method. Two simulation methods dissociate at the downslope rail current region. In Section III, we showed that the EMF term, which comes from rail inductance change due to lateral rail current movement is not a considerable term relative to EMFY-2. The reason for that is EMFY-1 has a smaller rail width. The reason for lower rail current at the downslope region in the control method is overestimated the VSE resistance due to 2-D approximation. EML model can be considered as discharging RL circuit at the downslope rail current region. Therefore, an overestimated lumped resistance causes a faster decay in the rail current. However, in EMFY-2 simulations the opposite is happened. The EMF term which is derived from rail current displacement is the dominant term; thus, $R_{backEMF}$ calculation without it results in a underestimated lumped resistance. Although the VSE resistance is overestimated also in EMFY-2 models, the effect of $R_{backEMF}$ is more significant. Therefore, rail current discharges slower in EMFY-2 control method simulations.

IV. Conclusion

The remarks which are obtained throughout the development of the simulation model can be listed as follows.

1) Beside from armature movement, the lateral rail current movement also generates an EMF which should be taken into account in EML simulations. Therefore, the correct approach to calculate EMF resistance is given in (11).
2) The boundaries where the L_{ext} and L_{int} are quite important. They should be calculated at the proposed surfaces in order to reduce to error that comes with the hybrid simulation method. The surface which is illustrated in Fig. 8 can be used to calculate the system inductance which did not covered by 3-D FEM in the hybrid simulation model.
3) VSE resistance calculation made with 2-D approximation overestimates the actual VSE resistance by 40%. Quasi-transient 3-D FEM analysis is a good alternative for VSE resistance modeling.
4) Hybrid model such as 3-D FEM and lumped circuit combination can be used for EML simulations effectively, since it decreases computational complexity where the error due to approximations is tolerable.

Acknowledgment

The authors would like to thank the other ASELSAN Team members whose support made this article possible.

References

[1] J. Wey, P. Lehmann, and H. Peter, "Des.3 MJ-railgun experimental results at ISL," *IEEE Trans. Magn.*, vol. 31, no. 1, pp. 371–376, Jan. 1995.
[2] S. Hundertmark, G. Vincent, F. Schubert, and J. Urban, "The NGL-60 railgun," *IEEE Trans. Plasma Sci.*, vol. 47, no. 7, pp. 3327–3330, Jul. 2019.
[3] F. Deadrick, R. Hawke, and J. Scudder, "MAGRAC—A railgun simulation program," *IEEE Trans. Magn.*, vol. 18, no. 1, pp. 94–104, Jan. 1982.
[4] G. E. Rolader, L. D. Thornhill, J. H. Batteh, and J. J. Scanlon, "Electromagnetic gun circuit analysis code (EGCAC)," *IEEE Trans. Magn.*, vol. 29, no. 1, pp. 499–504, Jan. 1993.
[5] J. Wey, E. Spahn, and M. Lichtenberger, "Railgun modeling with the P-Spice code," *IEEE Trans. Magn.*, vol. 33, no. 1, pp. 619–624, Jan. 1997.
[6] K. Hsieh, "A Lagrangian formulation for mechanically, thermally coupled electromagnetic diffusive processes with moving conductors," *IEEE Trans. Magn.*, vol. 31, no. 1, pp. 604–609, Jan. 1995.
[7] G.-H. Wang, L. Xie, Y. He, S.-Y. Song, and J.-J. Gao, "Moving mesh FE/BE hybrid simulation of electromagnetic field evolution for railgun," *IEEE Trans. Plasma Sci.*, vol. 44, no. 8, pp. 1424–1428, Aug. 2016.
[8] S. Tan, J. Lu, B. Li, Y. Zhang, and Y. Jiang, "A new finite-element method to deal with motion problem of electromagnetic rail launcher," *IEEE Trans. Plasma Sci.*, vol. 45, no. 7, pp. 1374–1379, Jul. 2017.
[9] K.-T. Hsieh and V. Thiagarajan, "A novel split-domain iteration scheme for solution of electromagnetic diffusion problems modeled by the hybrid finite-element–boundary-element formulation," *IEEE Trans. Magn.*, vol. 45, no. 1, pp. 587–590, Jan. 2009.
[10] P. Zuo, Y. Geng, J. Li, and J. Yuan, "An approach for eddy-current calculation in railguns based on the finite-element method," *IEEE Trans. Plasma Sci.*, vol. 43, no. 5, pp. 1592–1596, May 2015.
[11] Q.-H. Lin and B.-M. Li, "Numerical simulation of interior ballistic process of railgun based on the multi-field coupled model," *Defence Technol.*, vol. 12, no. 2, pp. 101–105, Apr. 2016. [Online]. Available: http://www.sciencedirect.com/science/article/pii/S2214914716000064
[12] H. Shatoff, D. Pearson, and A. Kull, "Simulation of dynamic armature motion in a railgun with coupling of electromagnetic, thermal and structural effects using shifted finite element fields," in *Proc. IEEE Pulsed Power Conf.*, Jun. 2005, pp. 253–256.
[13] K. Dai, Y. Yang, Q. Yin, and H. Zhang, "Theoretical model and analysis on the locally concentrated current and heat during electromagnetic propulsion," *IEEE Access*, vol. 7, pp. 164856–164866, 2019.
[14] S. Hundertmark and M. Roch, "Transient 3-D simulation of an experimental railgun using finite element methods," in *Proc. 16th Int. Symp. Electromagn. Launch Technol.*, May 2012, pp. 1–5.
[15] O. Liebfried, M. Schneider, T. Stankevic, S. Balevicius, and N. Zurauskiene, "Velocity-induced current profiles inside the rails of an electric launcher," *IEEE Trans. Plasma Sci.*, vol. 41, no. 5, pp. 1520–1525, May 2013.
[16] T. Stankevic, M. Schneider, and S. Balevicius, "Magnetic diffusion inside the rails of an electromagnetic launcher: Experimental and numerical studies," *IEEE Trans. Plasma Sci.*, vol. 41, no. 10, pp. 2790–2795, Oct. 2013.
[17] D. Ceylan, M. Karagoz, Y. Cevik, B. Yildirim, H. Polat, and O. Keysan, "Simulations and experiments of EMFY-1 electromagnetic launcher," *IEEE Trans. Plasma Sci.*, vol. 47, no. 7, pp. 3336–3343, Jul. 2019.
[18] M. Karagoz *et al.*, "ASELSAN electromagnetic launch laboratory: First shot," *IEEE Trans. Plasma Sci.*, vol. 48, no. 4, pp. 802–807, Apr. 2020.
[19] M. Karagoz *et al.*, "Aselsan EMFY-1 electromagnetic launcher: First experiments," in *Proc. IEEE 21st Int. Conf. Pulsed Power (PPC)*, Jun. 2017, pp. 1–3.

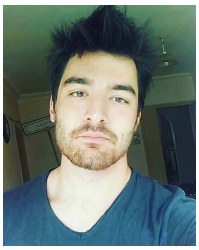

Nail Tosun (Graduate Student Member, IEEE) received the B.Sc. degree from the Department of Electrical and Electronics Engineering, Middle East Technical University (METU), Ankara, Turkey, in 2019, where he is currently pursuing the M.Sc. degree.

His current research interests include electromagnetic FEM analysis, optimization of electrical machines, and power electronics.

Hakan Polat (Member, IEEE) received the B.Sc. degree from the Department of Electrical and Electronics Engineering, Middle East Technical University (METU), Ankara, Turkey, in 2018, where he is currently pursuing the M.Sc. degree.

His current research interests include electromagnetic launchers, pulsed-power sources, renewable energy, and wireless power transfer.

Doğa Ceylan received the B.Sc. and M.Sc. degrees from the Department of Electrical and Electronics Engineering, Middle East Technical University (METU), Ankara, Turkey, in 2016 and 2018, respectively. He is currently pursuing the Ph.D. degree with the Electromechanics and Power Electronics Group, Eindhoven University of Technology, Eindhoven, The Netherlands.

His current research interests focus on the design and optimization of electrical machines, electric vehicles, and electromagnetic launchers.

Mustafa Karagöz received the B.Sc. and M.Sc. degrees from the Department of Electrical and Electronics Engineering, Middle East Technical University (METU), Ankara, Turkey, in 2010 and 2014, respectively.

Since 2010, he has been with ASELSAN Inc., Ankara, where he has been a Technical Project Manager in the Electromagnetic (EM) Railgun Project since 2014. His current research interests include EM launcher and pulsed power technologies.

Baran Yildirim received the B.Sc. degree from the Department of Mechanical Engineering, Middle East Technical University (METU), Ankara, Turkey, in 2008, and the master's and Ph.D. degrees from Northeastern University, Boston, MA, USA, in 2010 and 2013, respectively.

He is currently an Analysis and Test Engineer with ASELSAN Inc., Ankara. His current research interests include solid mechanics, impact mechanics, finite-element analysis, modeling of structural and dynamic systems, and dynamic measurement of structures.

İbrahim Güngen received the B.Sc. degree in electrical and electronics engineering from Middle East Technical University (METU), Ankara, Turkey, in 2017, where he is currently pursuing the M.Sc. degree with the Electrical and Electronics Engineering Department.

He is also an Electronics Design Research and Development Engineer with ASELSAN Inc. His current research interests include electromagnetic launchers and pulsed-power sources.

Ozan Keysan (Member, IEEE) received the master's degree from Middle East Technical University (METU), Ankara, Turkey, in 2008, and the Ph.D. degree from the University of Edinburgh, Edinburgh, Scotland, in 2014.

He is currently an Assistant Professor with the Electrical and Electronics Engineering Department, METU. His current research interests include renewable energy, design and optimization of electrical machines, smart grids, superconducting machines, and permanent-magnet machines.